Nano Research

Open Access

Research Article

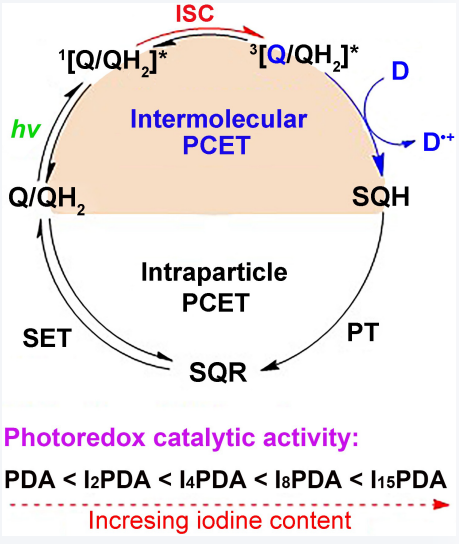
Iodinated polydopamine for visible-light photoredox catalysis

Chanyoung Jung[1,§], Hoyun Kim[1,§], Dokyeong Lee[1], Songyi Han[1], Sung Ho Yang[2], and Jungkyu K. Lee[1]✉

[1] Department of Chemistry and Green-Nano Materials Research Center, Kyungpook National University, Daegu 41566, Republic of Korea
[2] Department of Chemistry Education, Korea National University of Education (KNUE), Cheongju 28173, Republic of Korea
§ Chanyoung Jung and Hoyun Kim contributed equally to this work.

Cite this article: *Nano Research*, **2026**, *19*, 94908814. https://doi.org/10.26599/NR.2026.94908814

ABSTRACT: We demonstrated the photoredox catalytic activity of iodine-functionalized polydopamines (IPDAs) with varying iodine contents under green- and red-light irradiation in aqueous solution. IPDAs were readily prepared through post-polymerization iodination of PDA and characterized by X–ray photoelectron spectroscopy, UV–vis spectroscopy, FT–IR spectroscopy, and dynamic light scattering. Compared with intact PDA, IPDAs exhibited enhanced photocatalytic performance in radical photopolymerization of water-soluble acrylate monomers in the presence of triethanolamine. In particular, **I_{15}PDA** showed the highest activity under both green and red light, whereas intact PDA was essentially inactive under red-light irradiation. Kinetic analysis, reaction quantum yield, initiation efficiency, and monomer-scope studies consistently confirmed the superior catalytic performance of **I_{15}PDA**. Phosphorescence intensity increased with iodine content, indicating enhanced intersystem crossing via the heavy-atom effect. These findings establish iodine functionalization as an effective strategy to enhance the photoredox activity of PDA and provide fundamental mechanistic insights that enable the rational design of melanin-inspired organic photocatalysts.



KEYWORDS: organic photoredox catalyst, heavy-atom effect, functionalized polydopamine, red-light photoredox catalyst, photoinitiated radical polymerization

1 Introduction

Polydopamine (PDA) is a synthetic melanin-like polymer, inspired by the adhesive proteins of mussels [1, 2]. PDA has attracted considerable attention owing to its facile formation through the oxidative polymerization of dopamine under mild aqueous conditions [3]. The resulting polymer consists of a complex network primarily composed of 5,6-dihydroxyindole (QH_2), 5,6-indolequinone (Q), and dopamine-derived units. This chemical architecture imparts PDA with unique physicochemical properties, such as strong adhesion to diverse substrates, metal chelation, broadband light absorption, redox activity, and free-radical inhibition [4, 5]. Although the precise molecular structure of PDA remains an active subject of investigation, it is generally regarded as a heterogeneous polymer composed of the oligomeric units interconnected through non-covalent interactions, including π–π stacking, cation–π interactions, and hydrogen bonding [3, 6, 7].

Because of these versatile properties, PDA has found widespread applications across multiple fields. For example, PDA coatings have been widely used as universal surface modifiers for metals, polymers, and inorganic materials [8, 9]. In addition, the abundant catechol groups enable pre- and post-polymerization through Michael-type addition and/or Schiff-base reactions, allowing the incorporation of diverse functional molecules [10–13]. PDA has therefore been applied in areas including antibacterial coatings, drug/protein delivery, biosensing, photothermal therapy, catalysis, and energy conversion/storage [14–19]. Notably, PDA, as a biocompatible material with low cytotoxicity, has also been explored for biomedical applications such as cell encapsulation and cell surface engineering, where the biocompatibility and mild polymerization conditions allow conformal coating of living cells and biological substrates [20, 21]. For example, Choi and co-workers successfully demonstrated the encapsulation of individual living cells with a polymeric film by first coating the cell surface with PDA, followed by immobilization of a polymerization initiator

Received: March 31, 2026; **Revised:** May 2, 2026
Accepted: May 6, 2026

✉Address correspondence to jkl@knu.ac.kr

and subsequent surface-initiated polymerization [22]. The resulting polymer-coated cells exhibited suppressed cell-division activities and a prolonged lag phase.

PDA also exhibits intriguing photoactive and photoredox properties [23]. Especially, the broad absorption spectrum extending from the UV to the near-infrared region enables PDA to interact efficiently with visible light [24, 25]. For example, Meredith and co-workers demonstrated protonic electrical conductivity arising from the formation of semiquinone radical anion (SQR) species, whose concentration increases via proton-coupled electron transfer (PCET) between QH_2 and Q units (i.e., intraparticle PCET) under visible-light irradiation [26]. Stenzel and co-workers employed this mechanism to explain the visible-light photoredox catalytic activity of PDA in DMSO, where free-radical polymerization is initiated by phenyl radical species generated through single-electron transfer between diphenyliodonium (electron-accepting co-initiator) and SQR (electron donor) produced via intraparticle PCET [27]. Meanwhile, we reported visible-light photoredox catalysis of PDA (aq) in the presence of triethanolamine (TEOA, electron-donating co-initiator) and proposed that intermolecular PCET between the excited state of the Q moiety and TEOA plays a key role in initiating free-radical polymerization [28].

Despite these advances, the mechanism of visible light-induced photoredox catalysis of PDA remains unclear, and further systematic investigations are still required to comprehensively understand it. In this context, elucidating the relationship between its structure and photocatalytic activity will not only provide deeper mechanistic insight, but also enable the development of more efficient PDA-based photoredox catalysts with broader practical applications, such as synthetic chemistry and *in vivo* bioconjugation. In addition, red-light photoredox catalysis has emerged as a compelling alternative to green-light systems, owing to its reduced phototoxicity and byproduct formation, enhanced penetration depth, and wavelength-selective reactivity [29–32]. For example, red-light irradiation enabled erythrocyte surface labeling cells in whole blood, whereas blue-light irradiation exhibited poor photoredox catalytic activity, due to limited penetration [31].

Herein, we synthesized iodine-functionalized PDAs (IPDAs) with varying iodine contents and then studied their photoredox catalytic performance under green- and red-light irradiation. The photocatalytic activities of IPDAs were evaluated through free-radical photopolymerization of acrylate monomers in the presence of TEOA in aqueous solution. The radical polymerization was employed as a model reaction because its high reactivity and pseudo-first-order behavior provide an ideal platform for kinetic modeling and mechanistic studies of the photoredox catalysis. Furthermore, this versatile polymerization strategy is applicable to intracellular polymerization, chemobiosensors, single-cell nanoencapsulation, and the fabrication of biomedical scaffolds for tissue engineering and drug delivery [33–36].

2 Results and discussion

2.1 Synthesis and characterization of iodinated polydopamine (IPDA) particles

IPDAs were synthesized by post-polymerization modification (Fig. 1). Initially, PDA was prepared by dissolving dopamine hydrochloride (100 mg, 0.53 mmol) in 50 mL of a pH 11 buffer

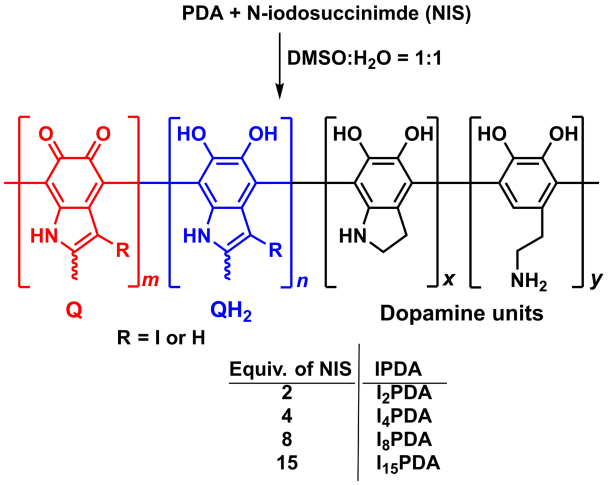


Figure 1 Schematic depiction of the synthesis of IPDAs.

solution. Without employing additional reagents, the pH gradually adjusted to approximately 8.5. After shaking at 100 rpm for 60 days, the resulting solution (30 mL, corresponding to 0.32 mmol based on dopamine hydrochloride) was subjected to iodination by treatment with N-iodosuccinimide (NIS) dissolved in DMSO (30 mL) at room temperature for 24 h under an argon atmosphere [37]. The amount of NIS was varied as follows: 2 equiv. (0.63 mmol) for **I_2PDA**, 4 equiv. (1.26 mmol) for **I_4PDA**, 8 equiv. (2.52 mmol) for **I_8PDA**, and 15 equiv. (4.73 mmol) for **I_{15}PDA**. The solvents were removed under reduced pressure by lyophilization for 36 h. The resulting powder was purified with ethanol to remove unreacted and residual species, including succinimide derivatives and iodine-derived species generated from NIS. Specifically, the powder was dispersed in ethanol (6 mL) by vortexing for 10 s, followed by sonication for 30 s. The suspension was then centrifuged at 1350 rpm for 1 min, and the supernatant was discarded. This washing procedure was repeated six times, and the absence of residual species in the supernatant was confirmed by ultraviolet–visible (UV–vis) analysis. For example, after a single wash of crude **I_{15}PDA**, the supernatant exhibited strong absorption bands in the 250–550 nm range, attributable to succinimide and iodine derivatives (Fig. S1 in the Electronic Supplementary Material (ESM)). In contrast, these characteristic absorption bands disappeared upon six washing cycles. After lyophilization of the precipitate, the purified IPDA was obtained as a black powder with yields of 82 (±1) mg for **I_2PDA**, 87 (±1) mg for **I_4PDA**, 99 (±4) mg for **I_8PDA**, and 105 (±1) mg for **I_{15}PDA** based on three independent syntheses.

While the precise structure of PDA remains under debate due to its inherent complexity and characterization challenges, it is generally accepted that PDA is primarily composed of QH_2, Q, and dopamine units [7]. Thus, IPDAs were carefully characterized by UV–vis spectrometry, X-ray photoelectron spectroscopy (XPS), particle size analysis, and Fourier transform infrared (FT-IR) spectroscopy. The XPS spectra of IPDAs revealed characteristic iodine peaks at 631.8–632.8 eV for I $3d_{3/2}$, and 620.3–621.2 eV for I $3d_{5/2}$ [38], which were absent in intact PDA (Fig. 2(a)). Furthermore, deconvolution analysis exhibited a noticeably higher atomic percentage of the I 3d signal for **I_{15}PDA** indicating a greater iodine content than that of **I_2PDA**. For example, normalization of the I 3d to C 1s atomic ratio showed that **I_{15}PDA** contained approximately 4.4-fold more iodine than **I_2PDA** (Fig S2 in the ESM). These results

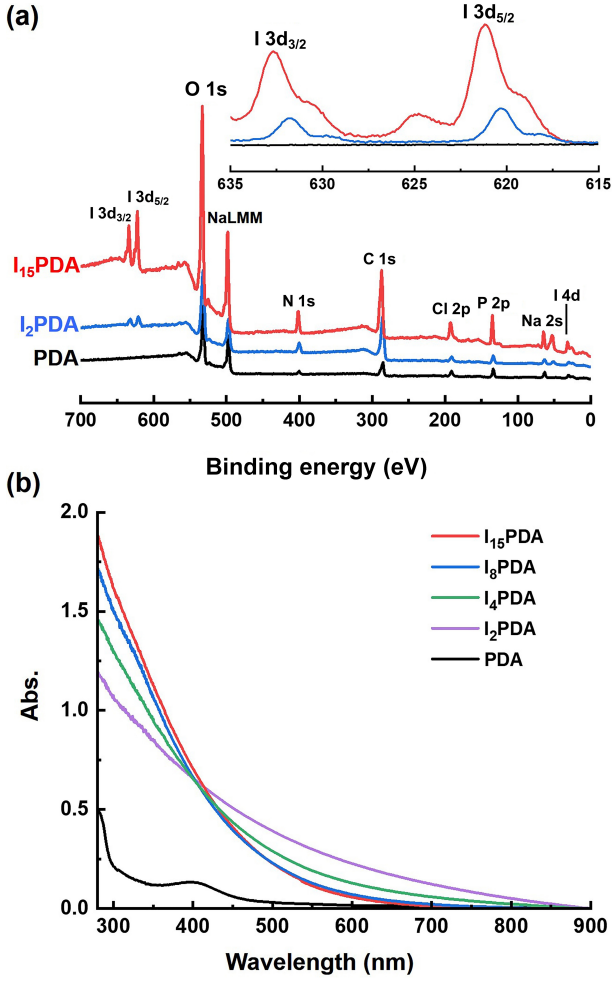


Figure 2 Characterization of IPDAs: (a) XPS spectra of PDA, **I_2PDA**, and **I_{15}PDA** and (b) UV–vis spectra of PDA and IPDAs.

confirm the successful incorporation of iodine into the PDA structure. Based on prior literature, we assume that iodination predominantly occurs at the C3 position of the indole moieties [39]. Furthermore, the amines derived from dopamine units participate in non-covalent interactions (e.g., cation–π interactions) within the PDA framework [8], which significantly reduces their nucleophilicity. Although these protonated amines can be deprotonated under alkaline conditions (pH > 10) [8], the reactions in this study were conducted at pH 8.5, where the amines are predominantly protonated. Consequently, electrophilic iodination at the amine sites is unlikely to occur. We further hypothesize that undesired iodinated amine species promotes disassembly of the PDA framework, leading to their removal during washing processes.

Dynamic light scattering analysis of aqueous IPDA solutions (0.025 w/v%) exhibited an inverse relationship between particle size and the amount of NIS added. For example, the mean diameters were 148 (±57) nm for **I_{15}PDA**, 253 (±16) nm for **I_8PDA**, 448 (±45) nm for **I_4PDA**, 594 (±112) nm for **I_2PDA**, and 847 (±80) nm for intact PDA (Fig. S3(a) in the ESM). We suggest that iodination disrupts the non-covalent interactions within PDA, as evidenced by the observed decrease in particle size following treatment with iodine (aq) (Fig. S3(b) in the ESM).

The UV–vis spectra of IPDAs (aq) showed significantly enhanced absorption intensity across the entire spectral range compared with intact PDA (aq) at equivalent concentrations.

Specifically, at a concentration of 0.011 w/v%, the absorbance of intact PDA at 400 nm was 0.13, while the IPDAs demonstrated substantially higher values exceeding 0.7 (Fig. 2(b)). This enhancement is presumably attributed to iodination of the PDA structure. For IPDAs, however, the absorption intensity above 400 nm gradually decreased with increasing iodine incorporation. For example, at 550 nm, the absorbance values were 0.4 for **I_2PDA**, 0.25 for **I_4PDA**, and 0.1 for both **I_8PDA** and **I_{15}PDA**. Notably, this trend contrasts with the observed photoredox catalytic activity. This suggests that absorptivity is not the primary determinant of the catalytic performance, as discussed in detail below. Furthermore, the FT-IR spectrum of **I_{15}PDA** exhibited characteristic bands of PDA at 3200–3500 cm^{-1} corresponding to O–H and N–H stretching vibrations, 2846–2920 cm^{-1} attributed to C–H stretching vibrations, and 1475–1600 cm^{-1} assigned to N–H bending and aromatic C=C stretching (Fig. S4 in the ESM) [40].

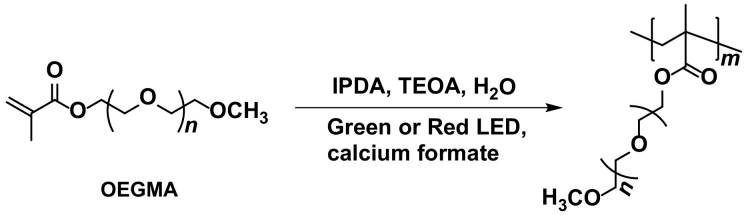
2.2 Green- or red-light-induced photopolymerization

Photoinitiated, free-radical polymerization was employed as a model reaction to evaluate the photoredox catalytic performance of IPDAs (aq.), due to its fast and well-defined reaction kinetics. Oligo(ethylene glycol) methyl ether methacrylate (OEGMA) was used as the water-soluble, biocompatible monomer, while TEOA served as both an electron donor and a co-initiator [41]. The free-radical photopolymerization of OEGMA was carried out under green (520 ± 30 nm, 4.2 $W{\cdot}cm^{-2}$) or red light-emitting diode (LED) (660 ± 30 nm, 5.9 $W{\cdot}cm^{-2}$) irradiation under various reaction conditions, including different atmospheres and concentrations of IPDAs. Calcium formate was employed as an internal standard for ^{1}H NMR analysis, as the methyl proton signal of OEGMA partially overlapped with the broad signals from the ethylene glycol moieties, leading to an underestimation of the monomer conversion. The presence of calcium formate had a negligible effect on the polymerization.

Under green-light irradiation for 1 h, IPDAs exhibited superior photoredox catalytic performance relative to intact PDA. At a concentration of 0.022 w/v%, PDA achieved 69% ± 3.8% monomer conversion with an apparent first-order reaction rate (k_{app}) of 0.1×10^{-4} s^{-1}, whereas IPDAs yielded ≥ 77% monomer conversion ($k_{app} \geq 3.0(\pm0.4) \times 10^{-4}$ s^{-1}) (Table 1, entries 1–5, Fig. S5(a) in the ESM) under identical conditions. Notably, increasing the NIS concentrations resulted in a progressive increase in both monomer conversion and k_{app} (Fig. 3(a)). Accordingly, **I_{15}PDA** showed the highest catalytic activity, achieving 96% ± 0.6% of monomer conversion ($k_{app} = 13(\pm0.3) \times 10^{-4}$ s^{-1}), outperforming **I_4PDA** (89% ± 0.6%) and **I_8PDA** (93% ± 0.1%) (Table 1, entries 3–5). Increasing the concentration of **I_{15}PDA** led to a slight acceleration of polymerization (Fig. 3(b)), with k_{app} values of $21(\pm1.4) \times 10^{-4}$ s^{-1} at 0.066 w/v%, $24(\pm0.5) \times 10^{-4}$ s^{-1} at 0.110 w/v%, and $28(\pm0.5) \times 10^{-4}$ s^{-1} at 0.154 w/v% (Table 1, entries 6–8, Fig. S5(b) in the ESM). However, intact PDA did not reach comparable activity even at higher concentration; for example, a monomer conversion of 77% ± 1.5% ($k_{app} = 2.0(\pm0.7) \times 10^{-4}$ s^{-1}) was obtained at 0.066 w/v% (Table 1, entry 9, Fig. S5(b) in the ESM). Control experiments confirmed that no polymerization occurred in the absence of either the photocatalyst or light irradiation (Table 1, entries 10 and 11, Fig. S5(c) in the ESM).

Under red-light irradiation, IPDAs exhibited dramatically increased reactivity compared with intact PDA. No monomer conversion was observed for intact PDA (0.066 w/v%), **I_2PDA**

Table 1 Investigation of photoinitiated, free-radical polymerization of OEGMA with different IPDAs under various reaction conditions using green LED (520 ± 30 nm, 4.2 W·cm^{-2}) or red LED (660 ± 30 nm, 5.9 W·cm^{-2}) irradiation[a]



Entry	Type of PDA	Conc. (w/v%)	[OEGMA]:[TEOA](mM)	Conv.[b,c](%)	k_{app}[b,c](×10^{-4} s^{-1})	Irrad.time (h)	LED source	Atm.
1	PDA	0.022	500:50	69 ± 3.8	0.1 ± < 0.1	1	Green	Air
2	**I_2PDA**	0.022	500:50	78 ± 1.0	3 ± 0.4	1	Green	Air
3	**I_4PDA**	0.022	500:50	89 ± 0.6	7 ± 0.6	1	Green	Air
4	**I_8PDA**	0.022	500:50	93 ± 0.1	11 ± 0.9	1	Green	Air
5	**I_{15}PDA**	0.022	500:50	96 ± 0.6	13 ± 0.3	1	Green	Air
6	**I_{15}PDA**	0.066	500:50	97 ± 0.6	21 ± 1.4	1	Green	Air
7	**I_{15}PDA**	0.110	500:50	98 ± 0.1	24 ± 0.5	1	Green	Air
8	**I_{15}PDA**	0.154	500:50	98 ± 0.1	28 ± 0.5	1	Green	Air
9	PDA	0.066	500:50	77 ± 1.5	2 ± 0.7	1	Green	Air
10	None	0	500:50	0	0	4	Green	Air
11	**I_{15}PDA**	0.066	500:50	0	0	12	None	Air
12	**PDA**	0.066	500:50	0	0	12	Red	Air
13	**I_2PDA**	0.022	500:50	0	0	3	Red	Air
14	**I_4PDA**	0.022	500:50	0	0	3	Red	Air
15	**I_8PDA**	0.022	500:50	4 ± 2.1	< 0.1	3	Red	Air
16	**I_{15}PDA**	0.022	500:50	64 ± 5.6	0.1 ± < 0.1	3	Red	Air
17	**I_{15}PDA**	0.066	500:50	98 ± 0.1	4 ± 0.4	3	Red	Air
18	**I_{15}PDA**	0.110	500:50	98 ± 0.1	4 ± 0.4	3	Red	Air
19	**I_{15}PDA**	0.154	500:50	98 ± 0.6	5 ± 0.3	3	Red	Air
20	**I_{15}PDA**	0.066	500:30	95 ± 0.6	3 ± 0.2	3	Red	Air
21	**I_{15}PDA**	0.066	500:0	0	0	12	Red	Air
22	None	0	500:50	0	0	12	Red	Air
23	**I_{15}PDA**	0.066	500:50	97	3.8	3	Red	Ar[d]
24	**I_{15}PDA**	0.066	500:50	0	0	3	Red	O_2[d]

[a]Photopolymerization was typically conducted in a standard NMR tube sealed with a cap, containing 0.6 mL of H_2O under aerobic conditions at room temperature. [b]Monomer conversion (%) was determined by ^{1}H NMR spectroscopy using calcium formate as an internal standard. k_{app}: apparent first-order rate coefficient. [c]Data were reported as mean ± standard deviation (n = 3). [d]A J-Young NMR tube equipped with a valve was used for reactions under Ar (g) and O_2 (g) atmospheres. TEOA: triethanolamine.

(0.022 w/v%), or **I_4PDA** (0.022 w/v%) even after 3 h of irradiation (Table 1, entries 12–14, Fig. 3(c) and Fig. S6(a) in the ESM). In contrast, at 0.022 w/v%, **I_8PDA** and **I_{15}PDA** achieved 4% ± 2.1% ($k_{app} \leq 0.1 \times 10^{-4}$ s^{-1}) and 64% ± 5.6% ($k_{app} = 0.1 \times 10^{-4}$ s^{-1}) monomer conversion, respectively, after 3 h of irradiation (Table 1, entries 15 and 16, Fig. 3(c) and Fig. S6(a) in the ESM). Increasing the concentration of **I_{15}PDA** accelerated polymerization; however, the reactivity reached a plateau above 0.066 w/v% (Fig. 3(d)). For instance, monomer conversions of 98% ± < 0.1% ($k_{app} = 4(\pm0.4) \times 10^{-4}$ s^{-1}) and 98% ± 0.6% ($k_{app} = 5(\pm0.4) \times 10^{-4}$ s^{-1}) were obtained at 0.066 w/v% and 0.154 w/v%, respectively (Table 1, entries 17–19, Fig. S6(b) in the ESM). Decreasing the TEOA concentration slightly reduced the polymerization rate; for example, 30 mM TEOA afforded 95% ± 0.6% monomer conversion ($k_{app} = 3(\pm0.2) \times 10^{-4}$ s^{-1}) (Table 1, entries 17 and 20, Fig. S6(b) in the ESM). Negative control experiments confirmed that no polymerization occurred after 12 h of irradiation in the absence of either IPDAs or TEOA (Table 1, entries 21 and 22, Fig. S6(c) in the ESM). Notably, the molecular weights of PEGMA exceeded the upper calibration limit of gel permeation chromatography (GPC) (approximately $M_n \geq 767$ kDa, $Đ$ = 2.94) even at 30% monomer conversion (eluent: DMF containing 1% LiBr and PMMA standards) (Fig. S7 in the ESM).

We further examined whether the iodine sources could initiate polymerization. No monomer conversion was observed after 12 h of red-light irradiation in solutions containing NIS (333 mM) or I_2 (167 mM) with OEGMA (500 mM), either in the absence or presence of TEOA (50 mM). Similarly, no monomer conversion was detected when these solutions were irradiated for 12 h, either in the presence or absence of PDA (0.066 w/v%) (Table S1 in the ESM). These results indicate that the iodine sources alone do not

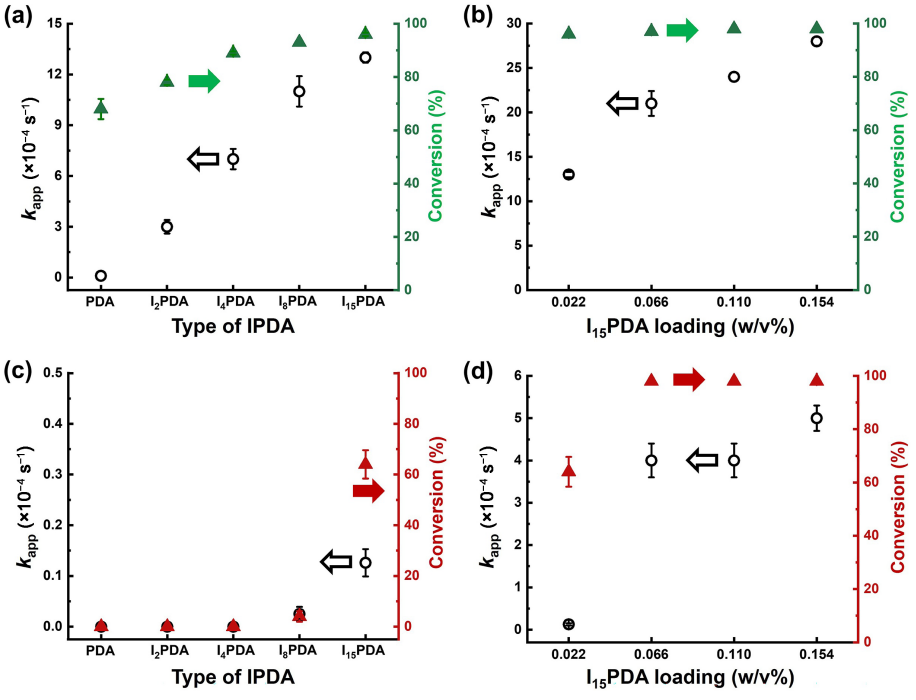


Figure 3 Photoredox catalytic activity as a function of photocatalyst type (IPDAs and PDA) and $\mathbf{I_{15}PDA}$ concentration under (a) and (b) green-light irradiation and (c) and (d) red-light irradiation.

initiate polymerization and that IPDAs serve as the active initiator/photocatalyst under red-light irradiation.

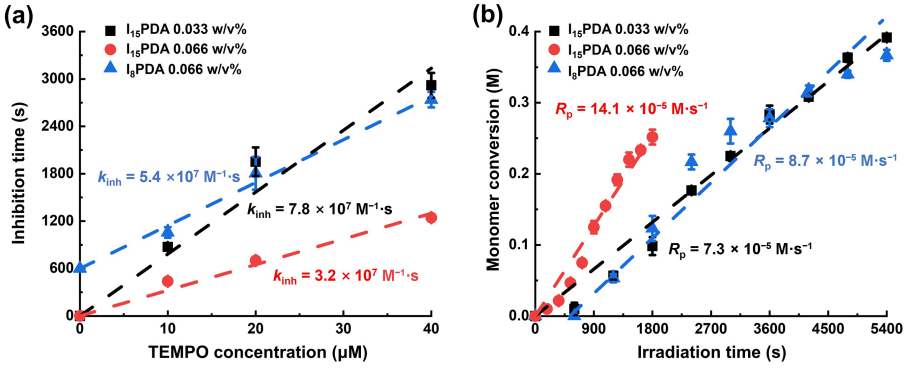
Under optimized conditions, we conducted the photoredox catalysis of $\mathbf{I_{15}PDA}$ under different atmospheres. Under an argon atmosphere, the photopolymerization rate was comparable to that under ambient conditions (Table 1, entries 17 and 23). However, under oxygen-rich conditions in a J-Young NMR tube, an induction period was observed, with polymerization proceeding only after the consumption of dissolved O_2 (Fig. S8 in the ESM). Notably, no monomer conversion was observed during 3 h of irradiation under continuous O_2 purging in a vial (Table 1, entry 24, Fig. S8 in the ESM). These results indicate that IPDA-based photoredox catalysis, similar to that of PDA, is inhibited by molecular oxygen [28]. Moreover, we conducted temporal control (on–off light) experiments under identical conditions to those in Table 1, entries 6 and 17. Considering the difference in reactivity under green and red light, irradiation intervals of 3 min (green light) and 20 min (red light) were applied. The light source was periodically switched on and off until the monomer conversion exceeded 85%, while no detectable monomer conversion occurred during the dark periods (Fig. S9 in the ESM). These results demonstrate that this polymerization proceeds with precise temporal control through light-mediated activation and deactivation.

2.3 Characterization of photopolymerization

To further characterize the photopolymerization mediated by IPDAs, several key parameters were determined. First, the reaction quantum yield (Φ_{rxn}) was measured to gain mechanistic insights into this photoredox process. Φ_{rxn} is defined as the number of products formed per photon absorbed at a given wavelength and is calculated as follows: $\Phi_{rxn} = (\text{mol}_{product})/(\text{photon flux}{\cdot}t{\cdot}f)$ [42]. Here, the number of product molecules formed was determined by ^{1}H NMR spectroscopy, the photon flux was measured by chemical actinometry using Reinecke's salt as a standard for 660 nm irradiation, t is the irradiation time for polymerization, and f is the fraction of light absorbed by IPDA (see the ESM for details) [43]. The Φ_{rxn} value increased with increasing iodine content and IPDA concentration (Fig. 4(c)). For example, under the red-light irradiation, Φ_{rxn} values of 42(±1) and 47(±4) were obtained for $\mathbf{I_{15}PDA}$ at 0.033 and 0.066 w/v%, respectively, while a value of 26 (±1) was observed for $\mathbf{I_8PDA}$ at 0.066 w/v% (Fig. S10 in the ESM). Given the chain- propagating nature of this photoinitiated free-radical polymerization, Φ_{rxn} values greater than 1 are expected, confirming the involvement of a chain process [44].

The initiation efficiency (Φ_i) of IPDAs was also determined, where Φ_i is defined as the ratio of the initiation rate (R_i) to the rate of light absorption (I_a) [42]. The R_i value was determined using the inhibition period method (see the ESM for details). Briefly, the concentration of 2,2,6,6-tetramethylpiperidine-1-oxyl (TEMPO), used as a radical inhibitor, was plotted against the inhibition time (t_{inh}) [45]. A linear increase in t_{inh} with increasing TEMPO concentration was observed (Fig. S11 in the ESM), and the R_i value was calculated from the slope of the plot ([TEMPO])/t_{inh}) (Fig. 4(a)). Under red-light irradiation in the presence of TEOA (50 mM) and OEGMA (500 mM), the R_i values were determined to be 1.3(±0.1) × 10^{-8} M·s^{-1} for $\mathbf{I_{15}PDA}$ at 0.033 w/v%, 3.1(±0.1) × 10^{-8} M·s^{-1} for $\mathbf{I_{15}PDA}$ at 0.066 w/v%, and 1.8(±0.1) × 10^{-8} M·s^{-1} for $\mathbf{I_8PDA}$ at 0.066 w/v% (Fig. 4(c)), indicating that the initiation rate increases with both iodine content and IPDA concentration.

The rate of light absorption (I_a) was determined using the Beer-Lambert law [$I_a = I_0(1 - 10^{-A})$], where I_0 is the incident light flux (determined by chemical actinometry) and A is the absorbance of IPDA (see the ESM for details) [42]. Under red-light irradiation, the calculated I_a values were 5.2(±0.3) × 10^{-7} M·s^{-1} for $\mathbf{I_{15}PDA}$ (0.033 w/v%), 8.6(±0.3) × 10^{-7} M·s^{-1} for $\mathbf{I_{15}PDA}$ (0.066 w/v%), and 8.3(±0.2) × 10^{-7} M·s^{-1} for $\mathbf{I_8PDA}$ (0.066 w/v%). Consequently, the Φ_i values were found to be 0.03(±0.002) for $\mathbf{I_{15}PDA}$ (0.033 w/v%), 0.04(±0.002) for $\mathbf{I_{15}PDA}$ (0.066 w/v%), and 0.02(±0.001) for $\mathbf{I_8PDA}$



(C)

Type of IPDA	Conc. (w/v%)	R_i (×10^{-8} M·s^{-1})	I_a (×10^{-7} M·s^{-1})	Φ_i (R_i /I_a)	R_p (×10^{-5} M·s^{-1})	Kinetic chain length	Φ_{rxn}
I_{15}PDA	0.033	1.3 (±0.1)	5.2 (±0.3)	0.03 (±0.002)	7.3 (±0.9)	5615 (±814)	42 (±1)
I_{15}PDA	0.066	3.1 (±0.1)	8.6 (±0.3)	0.04 (±0.002)	14.1 (±<0.1)	4548 (±150)	47 (±4)
I_8PDA	0.066	1.8 (±0.1)	8.3 (±0.2)	0.02 (±0.001)	8.7 (±0.2)	4833 (±290)	26 (±1)

Figure 4 Comparison of kinetic parameters of **I_8PDA** and **I_{15}PDA** in the presence of TEOA under ambient conditions: (a) plots of inhibition time versus TEMPO concentration, (b) correlation of propagation rate (R_p) with irradiation time, and (c) summary of the experimentally determined values. TEMPO: 2,2,6,6-tetramethylpiperidine-1-oxyl, R_i: initiation rate, I_a: light absorption, Φ_i: initiation efficiency, and Φ_{rxn}: reaction quantum yield.

(0.066 w/v%). These relatively low initiation efficiencies limit the overall polymerization rate (Fig. 4(c)).

The theoretical degree of polymerization (DP) was estimated from the kinetic chain length, defined as the ratio of the propagation rate (R_p) to the initiation rate (R_i) [46]. The R_p values, determined by ^{1}H NMR spectroscopy, increased with both IPDA concentration and iodine content. For example, R_p reached 7.3 (±0.9) × 10^{-5} M·s^{-1} for **I_{15}PDA** (0.033 w/v%), 14.1(±< 0.1) × 10^{-5} M·s^{-1} for **I_{15}PDA** (0.066 w/v%), and 8.7(±0.2) × 10^{-5} M·s^{-1} for **I_8PDA** (0.066 w/v%) (Fig. 4(b)). Accordingly, the calculated kinetic chain lengths were 5615(±814), 4548(±150), and 4833(±290), respectively (Fig. 4(c)). These results are consistent with the general principle that lower initiator rates lead to higher DP in free-radical polymerization, in agreement with the experimentally observed high molecular weights (M_n ≥ 767 kDa).

2.4 Investigation of monomer scope

We further evaluated the photopolymerization of various water-soluble monomers to assess the monomer scope using **I_{15}PDA** (0.066 w/v%) in the presence of TEOA under the optimized conditions described in Table 1. Under green-light irradiation for 1 h, **I_{15}PDA** afforded > 90% monomer conversion for all tested monomers (Figs. S12(a) and S12(b) in the ESM)). For example, monomer conversions of 95% (k_{app} = 24 × 10^{-4} s^{-1}) for 2-acrylamido-2-methyl-1-propanesulfonate (AMPS), 92% (k_{app} = 18 × 10^{-4} s^{-1}) for *N*-isopropylacrylamide (NIPAm), 91% (k_{app} = 7 × 10^{-4} s^{-1}) for 3-sulfopropyl methacrylate (SPMA), and 94% (k_{app} = 6 × 10^{-4} s^{-1}) for 2-hydroxyethyl methacrylate (HEMA) were achieved (Table 2, entries 1–4). In contrast, intact PDA afforded substantially lower monomer conversions of 51% (k_{app} = 0.4 × 10^{-4} s^{-1}) for AMPS, 10% (k_{app} = 0.2 × 10^{-4} s^{-1}) for NIPAm, and 59% (k_{app} = 0.6 × 10^{-4} s^{-1}) for SPMA. For HEMA, no detectable conversion was observed after 1 h, although 57% conversion was achieved after 4 h of irradiation.

Under red-light irradiation, intact PDA exhibited negligible monomer conversion for most monomers. In contrast, **I_{15}PDA** afforded appreciable monomer conversions, although lower than those observed under green-light irradiation (Figs. S12(c) and S12(d)). Specifically, **I_{15}PDA** achieved monomer conversions of 35% (k_{app} = 0.4 × 10^{-4} s^{-1}) for AMPS, 23% (k_{app} = 0.2 × 10^{-4} s^{-1}) for

Table 2 Investigation of monomer scope in the **I_{15}PDA**/TEOA system under aerobic conditions with green- or red-light irradiation[a]

Entry	Monomer	PC	Conv.[b] (%)	Irrad. time (h)	LED source
1	AMPS	**I_{15}PDA**	95	1	Green
		PDA	51	1	Green
2	NIPAm	**I_{15}PDA**	92	1	Green
		PDA	10	1	Green
3	SPMA	**I_{15}PDA**	91	1	Green
		PDA	59	1	Green
4	HEMA	**I_{15}PDA**	94	1	Green
		PDA	0	1	Green
		PDA	57	4	Green
5	AMPS	**I_{15}PDA**	35	3	Red
		PDA	0	3	Red
6	NIPAm	**I_{15}PDA**	23	3	Red
		PDA	0	3	Red
7	SPMA	**I_{15}PDA**	24	3	Red
		PDA	0	3	Red
8	HEMA	**I_{15}PDA**	16	3	Red
		I_{15}PDA	85	12	Red
		PDA	15	3	Red
		PDA	46	12	Red

[a]Photopolymerization was conducted in a standard NMR tube sealed with a cap under aerobic conditions at room temperature. The reaction solution consisted of **I_{15}PDA** (0.066 w/v%) or PDA (0.066 w/v%), TEOA (50 mM), and monomer (500 mM) dissolved in H_2O (total volume: 0.6 mL). [b]Monomer conversion (%) was determined by ^{1}H NMR spectroscopy using calcium formate as an internal standard. AMPS = 2-acrylamido-2-methyl-1-propanesulfonate, NIPAm = N-isopropylacrylamide, SPMA = 3-sulfopropyl methacrylate, and HEMA = 2-hydroxyethyl methacrylate.

NIPAm, 24% (k_{app} = 0.2 × 10^{-4} s^{-1}) for SPMA, and 16% (k_{app} = 0.2 × 10^{-4} s^{-1}) for HEMA after 3 h of irradiation (Table 2, entries 5–8). Notably, for HEMA, intact PDA afforded 15% (k_{app} = 0.1 × 10^{-4} s^{-1}) and 46% (k_{app} = 0.2 × 10^{-4} s^{-1}) monomer conversion after 3 and 12 h, respectively, whereas **I_{15}PDA** achieved 85% conversion (k_{app} = 0.5 × 10^{-4} s^{-1}) after 12 h (Table 2, entry 8). These results confirm that **I_{15}PDA** exhibits broad monomer compatibility and markedly enhanced photoredox catalytic performance compared with intact PDA under both green- and red-light irradiation.

2.5 Photophysical and electrochemical characterizations

We assume that the higher reactivity of IPDA compared with intact PDA is attributed to the heavy-atom effect. This photophysical phenomenon arises from the presence of heavy atoms (e.g., iodine and iridium), which enhance spin-orbit coupling and thereby increase the intersystem crossing (ISC) between the singlet and triplet excited states [47]. In organic photoredox catalysis, single-electron transfer (SET)—a key step—between electron donors and electron acceptors predominantly proceeds via the triplet excited state [48]. Thus, the efficiency of ISC plays a pivotal role in determining photoredox catalytic activity [49]. To support this hypothesis, we measured the phosphorescence spectra of IPDAs and PDA using time-resolved photoluminescence spectroscopy (FLS 1000, Edinburgh Instruments Ltd., UK) at 77 K. Notably, the intensity of phosphorescence, which reflects the population of the triplet excited state, serves as a useful indicator of ISC efficiency. Figure 5(a) exhibits the phosphorescence spectra of IPDAs and PDA at 0.011 w/v% in water. The phosphorescence maxima (λ_p) were observed at 546 nm for **I_{15}PDA**, 544 nm for **I_8PDA**, 532 nm for **I_4PDA**, 530 nm for both **I_2PDA** and PDA. Increasing iodine content resulted in a slight red shift of λ_p. The corresponding lifetimes, obtained from the major decay components, were 86 (±1.4) ms (57%) for **I_{15}PDA**, 96(±2.7) ms (59%) for **I_8PDA**, 92 (±2.4) ms (62%) for **I_4PDA**, 100(±3.3) ms (61%) for **I_2PDA**, and 121(±5.9) ms (77%) for PDA (Fig. 5(b)). These long lifetimes confirm that the observed emissions originate from phosphorescence [50]. In contrast, the fluorescence lifetimes of approximately 3 ns were observed as the major components for all samples (Table 3, Fig. S13 in the ESM). Notably, the phosphorescence intensity at λ_p increased progressively with iodine content in the order **I_{15}PDA** > **I_8PDA** > **I_4PDA** > **I_2PDA** > PDA. For example, the emission intensity of **I_{15}PDA** at λ_p was approximately threefold higher than that of PDA and about twofold higher than that of **I_4PDA**. Similarly, **I_8PDA** exhibited approximately twofold higher intensity than PDA and about 1.5-fold higher than **I_4PDA**. These results indicate that iodine incorporation enhances ISC efficiency, thereby increasing the triplet-state population and improving photoredox catalytic performance.

In addition to the heavy-atom effect, the thermodynamics and

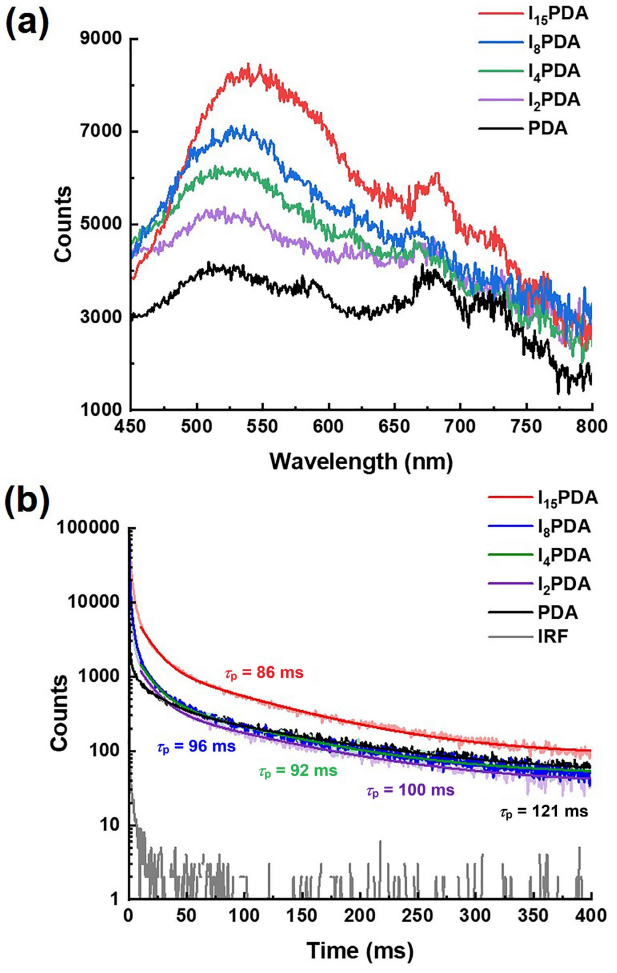


Figure 5 (a) Time-gated phosphorescence spectra of IPDAs (0.011w/v% in H_2O) and PDA (0.011 w/v% in H_2O) at 77 K with a delay time of 2 ms. (b) Phosphorescence decay profiles of IPDAs and PDA at 77 K, where solid lines represent the best-fit curves, and the lower gray line denotes the instrument response function (IRF).

Table 3 Summary of photophysical and electrochemical properties of IPDAs and PDA[a]

	I_{15}PDA	**I_8PDA**	**I_4PDA**	**I_2PDA**	PDA
$\lambda_{ex,vis}$ (nm)[a]	319	320	320	320	326
$\lambda_{F,vis}$ (nm)[a]	500	469	466	461	459
τ_F (ns)[a]	3 (±0.1, 78%) 19 (±0.8, 22%)	3 (±0.1, 80%) 17 (±0.8, 20%)	3 (±0.1, 77%) 14 (±0.9, 23%)	3 (±0.1, 83%) 16 (±0.5, 17%)	3 (±0.1, 79%) 17 (±0.5, 21%)
λ_p (nm)[a,b]	546	544	532	530	530
τ_p (ms)[a,b]	13 (±0.2, 43%) 86 (±1.4, 57%)	13 (±0.4, 41%) 96 (±2.7, 59%)	13 (±0.4, 38%) 92 (±2.4, 62%)	14 (±0.5, 39%) 100 (±3.3, 61%)	21 (±1.4, 23%) 121 (±5.9, 77%)
$E^{T1}_{0,0}$ (eV)	2.27	2.28	2.33	2.34	2.34
$E^{red}_{1/2}$ (V, SCE)[c]	−0.99	−0.89	−0.80	−0.78	−0.68
ΔG_{PET} (eV)[d]	−0.42	−0.53	−0.67	−0.70	−0.80

[a]Determined in 0.011 w/v% in H_2O. [b]Determined in cryogenic conditions. [c]Determined in 0.022 w/v% in pH 11 buffer (aq). [d]$\Delta G_{PET} = -[E^*_{red}(IPDA^*/IPDA^{\bullet-}) - E_{ox}(TEOA^{\bullet+}/TEOA)]$, $E^*_{red}(IPDA^*/IPDA^{\bullet-}) = E_{red}(IPDA/IPDA^{\bullet-}) + E^{T1}_{0,0}$, and $E_{ox}(TEOA^{\bullet+}/TEOA)$ = 0.86 eV.

kinetics of the photoinduced electron transfer (PET) process were investigated to elucidate the superior photoredox catalytic performance of **I_{15}PDA**. Because IPDAs in this work act as electron acceptors, the Gibbs free energy change for the PET (ΔG_{PET}) was determined using the following equation: $\Delta G_{PET} = -F[E^{*}_{red}(IPDA/IPDA^{\bullet-}) - E_{ox}(TEOA^{\bullet+}/TEOA)]$, where $E^{*}_{red}(IPDA/IPDA^{\bullet-}) = E_{red}(IPDA/IPDA^{\bullet-}) + E^{T1}_{0,0}$. Here, F is the Faraday constant, and $E^{T1}_{0,0}$ represents the triplet excited-state energy of IPDA, estimated from λ_p [48]. Furthermore, linear sweep voltammetry (LSV) was employed to determine the reduction potentials of IPDAs (see the ESM for details). The reduction potentials of IPDAs and PDA showed a decreasing trend: **I_{15}PDA** (−0.99 V), **I_8PDA** (−0.89 V), **I_4PDA** (−0.80 V), **I_2PDA** (−0.78 V), and PDA (−0.68 V) in aqueous solution (Fig. S14 in the ESM). The oxidation potential of TEOA was measured to be 0.86 eV in aqueous solution [28]. The triplet excited-state energies of IPDAs, estimated from phosphorescence spectra, showed a slight increase with decreasing iodine content: **I_{15}PDA** (2.27 eV), **I_8PDA** (2.28 eV), **I_4PDA** (2.33 eV), **I_2PDA** (2.34 eV), and PDA (2.34 eV) in aqueous solution. Consequently, the ΔG_{PET} values became less negative with increasing iodine content: PDA (−0.80 eV), **I_2PDA** (−0.70 eV), **I_4PDA** (−0.67 eV), **I_8PDA** (−0.53 eV), and **I_{15}PDA** (−0.42 eV) (Table 3). These results indicate that the thermodynamic driving force for PET follows the order: PDA > **I_2PDA** > **I_4PDA** > **I_8PDA** > **I_{15}PDA**. From a kinetic perspective, Stern-Volmer analysis suggests that the electron transfer between IPDAs and TEOA is likely diffusion-limited (Fig. S15 in the ESM), a common characteristic of intermolecular electron transfer processes in liquid solution [51, 52]. Consequently, the intrinsic electron-transfer kinetics cannot be decoupled from diffusion and are therefore not considered further. Notably, although **I_{15}PDA** is the least thermodynamically favorable for PET among the series, it exhibits the highest photoredox catalytic activity. Additionally, because the absorptivity above 500 nm decreases with increasing iodine content (Fig. 1(b)), these results indicate that the enhanced performance of **I_{15}PDA** arises primarily from the heavy-atom effect.

2.6 Photobleaching of I_{15}PDA

The photobleaching behavior of **I_{15}PDA** was investigated under different atmospheric conditions to support the proposed mechanism. Photobleaching was quantified by monitoring the decrease in integrated absorbance over time within the relevant spectral windows (490–550 nm for green light and 630–690 nm for red light), using 0.033 w/v% of **I_{15}PDA**. No photobleaching was observed in the dark under any conditions. Under green-light irradiation, the photobleaching rate followed the trend: oxygen-rich > air > argon. For example, after 4 h of irradiation in the presence of TEOA, photobleaching reached 85% under oxygen-rich conditions, 73% under ambient conditions, and 19% under argon (Fig. 6(a)). In the absence of TEOA, photobleaching reached 67%, 55%, and 20% under oxygen-rich, ambient, and argon atmospheres, respectively. A similar trend was observed under red-light irradiation, although the overall photobleaching rate was lower than that under green-light irradiation. For instance, after 10 h of irradiation in the presence of TEOA, photobleaching reached 73%, 68%, and 18% under oxygen-rich, ambient, and argon atmospheres, respectively (Fig. 6(b)). In the absence of TEOA, photobleaching reached 45%, 35%, and 20% for oxygen-rich, ambient, and argon atmospheres, respectively. Overall, **I_{15}PDA** exhibited behavior similar to that of PDA but with a higher photobleaching rate [28].

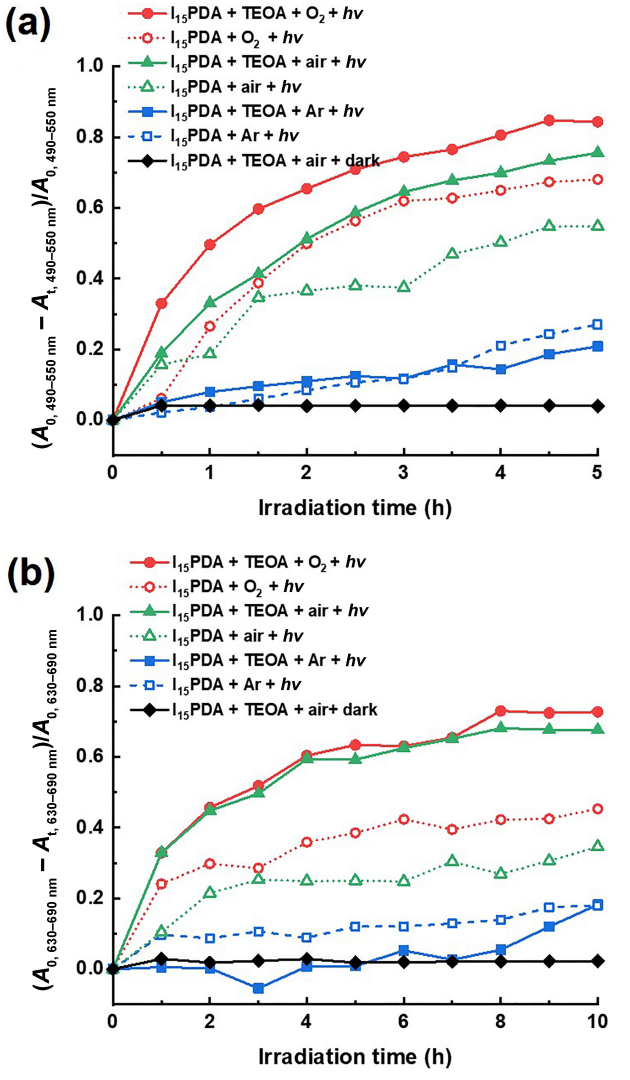


Figure 6 Photobleaching of **I_{15}PDA** (0.033 w/v% in H_2O) under (a) green- and (b) red-light irradiation across different experimental conditions.

These results suggest that molecular oxygen promotes photobleaching, thereby diminishing the photocatalytic activity of IPDA.

2.7 Plausible mechanism

We suggest the following photoredox catalytic mechanism based on these results (Fig. 7). Upon green- or red-light irradiation, the IPDA chains, consisting primarily of covalently linked QH_2 and Q units, are excited to the singlet excited state, $^1[Q/QH_2]^*$. This species subsequently undergoes intersystem crossing to the triplet excited state, $^3[Q/QH_2]^*$. In the presence of TEOA as an electron donor, a protonated semiquinone radical (SQH) is produced via intermolecular proton-coupled electron transfer (PCET) between $^3[Q/QH_2]^*$ and TEOA, where the excited Q unit accepts an electron from TEOA. The resulting SQH species rapidly deprotonates to form a semiquinone radical anion (SQR), stabilized by the negative charge of its conjugate base [53]. Notably, control experiments conducted in the dark indicate that although SQR can also be formed in the absence of light [26], it does not effectively initiate radical reactions in this system. The SQR species subsequently returns to the ground state $[Q/QH_2]$ through SET, completing the

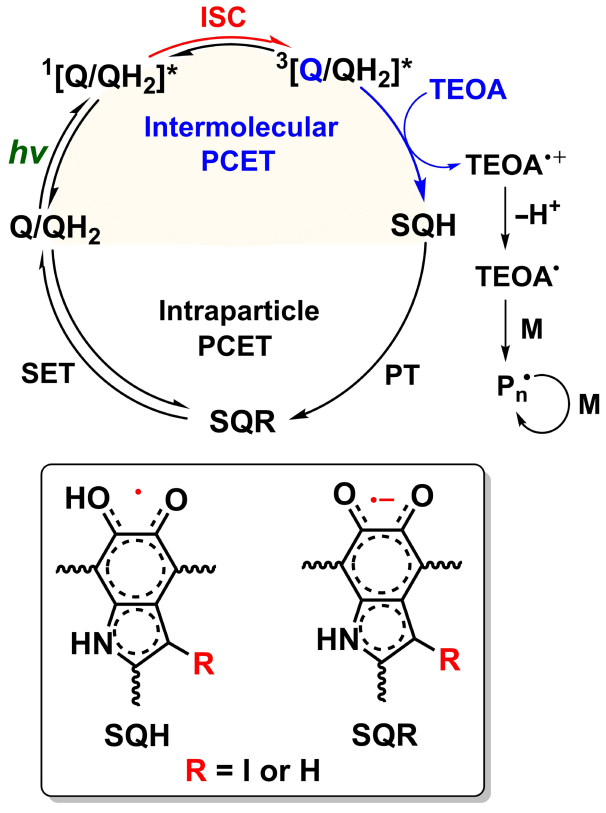


Figure 7 Plausible mechanism of photoredox catalysis of IPDA (aq) under green- or red-light irradiation. PCET = proton-coupled electron transfer; PT = proton transfer; SET = single-electron transfer.

intraparticle process. Concurrently, the oxidized TEOA forms an amino radical cation, which loses a proton to generate a reactive α-amino radical. This species serves as the primary initiator for the subsequent polymerization process.

3 Conclusions

In summary, we synthesized iodine-functionalized polydopamines bearing different iodine contents and systematically investigated their visible-light photoredox catalytic properties in aqueous solution. The IPDAs exhibited substantially higher photocatalytic activity than pristine PDA for free-radical photopolymerization under both green- and red-light irradiation, with **I_{15}PDA** showing the best overall performance. Notably, whereas pristine PDA displayed negligible activity under red light, **I_{15}PDA** enabled efficient polymerization, highlighting the significant impact of iodine incorporation on the photoredox behavior of PDA. Furthermore, **I_{15}PDA** exhibited photocatalytic efficiency comparable to that of eosin Y, a representative metal-free organic photoredox catalyst. Comprehensive photophysical and kinetic studies suggest that the enhanced photocatalytic activity of IPDAs arises primarily from the heavy-atom effect. Time-resolved phosphorescence measurements showed a progressive increase in triplet-excited state emission with increasing iodine content, suggesting more efficient intersystem crossing. In contrast, thermodynamic analysis revealed that the driving force for PET with TEOA became less favorable as iodine content increased. Thus, the superior activity of **I_{15}PDA** cannot be explained by electron-transfer thermodynamics alone. Instead, the enhanced performance is attributed primarily to the heavy-atom effect, which increases triplet-excited state population and thereby promotes photoredox catalysis. We envision that this work provides new mechanistic insights into the structure-photoreactivity relationship of PDA-based photocatalysts and demonstrates that halogen functionalization is an effective strategy for tuning their photoredox performance. Given the mild aqueous conditions, broad monomer scope, and ability to operate under red-light irradiation, IPDAs represent promising metal-free photoredox catalysts for applications in polymer synthesis, bio-related materials, and light-mediated functional materials design.

Electronic Supplementary Material: Supplementary material (characterizations, FT-IR spectra, ^{1}H NMR spectra, kinetic analysis, particle size analysis, LSV curves, and fluorescence decay curves) is available in the online version of this article at https://doi.org/10.26599/NR.2026.94908814.

Data availability

All data needed to support the conclusions in the paper are presented in the manuscript and the Electronic Supplementary Material. Additional data related to this paper may be requested from the corresponding author upon request.

Acknowledgements

This research was supported by the National Research Foundation of Korea (NRF) grant funded by the Korea government (MSIT) (Nos. RS-2023-00239038 and RS-2026-25469700).

Declaration of competing interest

All the contributing authors report no conflict of interests in this work.

Author contribution statement

C. J.: Data curation, investigation, methodology, validation, visualization, writing manuscript. H. K.: Investigation, methodology, validation, writing manuscript. D. L: Investigation, methodology, validation. S. H.: Investigation, methodology, validation. S. H. Y.: Software, supervision, visualization, writing. J. K. L.: Conceptualization, data curation, funding acquisition, investigation, methodology, supervision, validation, writing manuscript. All the authors have approved the final manuscript.

Use of AI statement

None.

References

[1] Lee, H.; Dellatore, S. M.; Miller, W. M.; Messersmith, P. B. Mussel-inspired surface chemistry for multifunctional coatings. *Science* **2007**, *318*, 426–430.

[2] Waite, J. H.; Tanzer, M. L. Polyphenolic substance of *Mytilus edulis*: Novel adhesive containing L-dopa and hydroxyproline. *Science* **1981**, *212*, 1038–1040.

[3] Hong, S.; Na, Y. S.; Choi, S.; Song, I. T.; Kim, W. Y.; Lee, H. Non-covalent self-assembly and covalent polymerization co-contribute to polydopamine formation. *Adv. Funct. Mater.* **2012**, *22*, 4711–4717.

[4] d'Ischia, M.; Napolitano, A.; Pezzella, A.; Meredith, P.; Buehler, M. Melanin biopolymers: Tailoring chemical complexity for materials design. *Angew. Chem., Int. Ed.* **2020**, *59*, 11196–11205.

[5] Chen, C. T.; Chuang, C.; Cao, J. S.; Ball, V.; Ruch, D.; Buehler, M. J. Excitonic effects from geometric order and disorder explain broadband optical absorption in eumelanin. *Nat. Commun.* **2014**, *5*, 3859.

[6] Hemmatpour, H.; De Luca, O.; Crestani, D.; Stuart, M. C. A.; Lasorsa, A.; van der Wel, P. C. A.; Loos, K.; Giousis, T.; Haddadi-Asl, V.; Rudolf, P. New insights in polydopamine formation via surface adsorption. *Nat. Commun.* **2023**, *14*, 664.

[7] Liebscher, J.; Mrówczynski, R.; Scheidt, H. A.; Filip, C.; Hădade, N. D.; Turcu, R.; Bende, A.; Beck, S. Structure of polydopamine: A never-ending story. *Langmuir* **2013**, *29*, 10539–10548.

[8] Lee, H. A.; Park, E.; Lee, H. Polydopamine and its derivative surface chemistry in material science: A focused review for studies at KAIST. *Adv. Mater.* **2020**, *32*, 1907505.

[9] Lee, H. A.; Ma, Y. F.; Zhou, F.; Hong, S.; Lee, H. Material-independent surface chemistry beyond polydopamine coating. *Acc. Chem. Res.* **2019**, *52*, 704–713.

[10] Ryu, J. H.; Messersmith, P. B.; Lee, H. Polydopamine surface chemistry: A decade of discovery. *ACS Appl. Mater. Interfaces* **2018**, *10*, 7523–7540.

[11] Wang, K.; Zhang, H. J.; Wang, M. X.; Li, Z. Y.; Wu, W.; Liu, P. C.; Liu, R. Q.; Gu, Z. P.; Li, Y. W.; Zhang, Z. Y. Bioadhesive polydopamine-vitamin A derivative hydrogels reprogram the wound microenvironment for scarless wound healing and hair follicle regeneration. *Mater. Horiz.* **2026**, *13*, 3489–3506.

[12] Heo, Y.; Ji, M.; Ryu, C. Y.; Kim, H.; Choi, I.; Kang, S. M.; Kim, M. Structural modifications on dopamine molecules toward polydopamine applications. *Eur. J. Org. Chem.* **2025**, *28*, e202401035.

[13] Choi, J.; Jeon, H.; Hwang, S.; Lee, H.; Hong, S.; Kang, K. Synthetic neuromelanin particles for metal-free photocatalysis. *Small* **2025**, *21*, e10311.

[14] Gao, S. P.; Zhang, D.; Pedrero, M.; Guo, Z. M.; Pingarrón, J. M.; Campuzano, S.; Zou, X. B. Advances and opportunities of polydopamine coating in biosensing: Preparation, functionality, and applications. *Coord. Chem. Rev.* **2024**, *501*, 215564.

[15] Liu, Y. L.; Ai, K. L.; Lu, L. H. Polydopamine and its derivative materials: Synthesis and promising applications in energy, environmental, and biomedical fields. *Chem. Rev.* **2014**, *114*, 5057–5115.

[16] Zou, Y.; Wang, T. Y.; Lin, X.; Yang, L.; Li, Y. W. Regulation of the light absorption and photothermal performance of melanin-like polymers. *Acc. Chem. Res.* **2025**, *58*, 2815–2829.

[17] Jia, T. K.; Wang, W. J.; Zhang, C. Q.; Zhang, L.; Wang, W. Z. Polydopamine-mediated contact-electro-catalysis for efficient partial oxidation of methane. *Angew. Chem., Int. Ed.* **2025**, *64*, e202413343.

[18] Xu, Y. T.; Hu, J. F.; Hu, J. J.; Cheng, Y. Y.; Chen, X. C.; Gu, Z. P.; Li, Y. W. Bioinspired polydopamine hydrogels: Strategies and applications. *Prog. Polym. Sci.* **2023**, *146*, 101740.

[19] Li, H.; Jia, Y.; Bai, S. W.; Peng, H. N.; Li, J. B. Metal-chelated polydopamine nanomaterials: Nanoarchitectonics and applications in biomedicine, catalysis, and energy storage. *Adv. Colloid Interface Sci.* **2024**, *334*, 103316.

[20] Yang, S. H.; Kang, S. M.; Lee, K. B.; Chung, T. D.; Lee, H.; Choi, I. S. Mussel-inspired encapsulation and functionalization of individual yeast cells. *J. Am. Chem. Soc.* **2011**, *133*, 2795–2797.

[21] Maurelli, A. M.; De Leo, V.; Catucci, L. Polydopamine-modified liposomes: Preparation and recent applications in the biomedical field. *ACS Omega* **2024**, *9*, 24105–24120.

[22] Kim, J. Y.; Lee, B. S.; Choi, J.; Kim, B. J.; Choi, J. Y.; Kang, S. M.; Yang, S. H.; Choi, I. S. Cytocompatible polymer grafting from individual living cells by atom-transfer radical polymerization. *Angew. Chem., Int. Ed.* **2016**, *55*, 15306–15309.

[23] Kim, J. H.; Lee, M.; Park, C. B. Polydopamine as a biomimetic electron gate for artificial photosynthesis. *Angew. Chem., Int. Ed.* **2014**, *53*, 6364–6368.

[24] Grieco, C.; Kohl, F. R.; Hanes, A. T.; Kohler, B. Probing the heterogeneous structure of eumelanin using ultrafast vibrational fingerprinting. *Nat. Commun.* **2020**, *11*, 4569.

[25] Sheng, W. B.; Li, B.; Wang, X. L.; Dai, B.; Yu, B.; Jia, X.; Zhou, F. Brushing up from "anywhere" under sunlight: A universal surface-initiated polymerization from polydopamine-coated surfaces. *Chem. Sci.* **2015**, *6*, 2068–2073.

[26] Mostert, A. B.; Rienecker, S. B.; Noble, C.; Hanson, G. R.; Meredith, P. The photoreactive free radical in eumelanin. *Sci. Adv.* **2018**, *4*, eaaq1293.

[27] Bailey, C. G.; Nothling, M. D.; Fillbrook, L. L.; Vo, Y.; Beves, J. E.; McCamey, D. R.; Stenzel, M. H. Polydopamine as a visible-light photosensitiser for photoinitiated polymerisation. *Angew. Chem., Int. Ed.* **2023**, *62*, e202301678.

[28] Kim, H.; Lee, D.; Jung, Y. J.; Yang, S. H.; Lee, H. J.; Lee, H. I.; Lee, J. K. Visible-light photoredox catalysis of polydopamine with triethanolamine in water. *Chem. Sci.* **2025**, *16*, 15499–15509.

[29] He, X. X.; Jin, S. L.; Dai, X. X.; Chen, L.; Xiang, L. H.; Zhang, C. F. The emerging role of visible light in melanocyte biology and skin pigmentary disorders: Friend or foe. *J. Clin. Med.* **2023**, *12*, 7488.

[30] Hossain, M. M.; Shaikh, A. C.; Kaur, R.; Gianetti, T. L. Red light-blue light chromoselective $C(sp^2)$–X bond activation by organic helicenium-based photocatalysis. *J. Am. Chem. Soc.* **2024**, *146*, 7922–7930.

[31] Buksh, B. F.; Knutson, S. D.; Oakley, J. V.; Bissonnette, N. B.; Oblinsky, D. G.; Schwoerer, M. P.; Seath, C. P.; Geri, J. B.; Rodriguez-Rivera, F. P.; Parker, D. L. et al. µMap-red: Proximity labeling by red light photocatalysis. *J. Am. Chem. Soc.* **2022**, *144*, 6154–6162.

[32] Zhang, T.; Pradhan, S.; Das, S. Red-light-mediated generation of radicals: Applications in organic synthesis, small-molecule activation, polymerization, and bio-related fields. *Angew. Chem., Int. Ed.* **2025**, *64*, e202501194.

[33] Geng, J.; Li, W. S.; Zhang, Y. C.; Thottappillil, N.; Clavadetscher, J.; Lilienkampf, A.; Bradley, M. Radical polymerization inside living cells. *Nat. Chem.* **2019**, *11*, 578–586.

[34] Rheem, H. B.; Kim, N.; Nguyen, D. T.; Baskoro, G. A.; Roh, J. H.; Lee, J. K.; Kim, B. J.; Choi, I. S. Single-cell nanoencapsulation: Chemical synthesis of artificial cell-in-shell spores. *Chem. Rev.* **2025**, *125*, 6366–6396.

[35] Kim, S.; Sikes, H. D. Radical polymerization reactions for amplified biodetection signals. *Polym. Chem.* **2020**, *11*, 1424–1444.

[36] Langer, R.; Vacanti, J. P. Tissue engineering. *Science* **1993**, *260*, 920–926.

[37] Carreño, M. C.; Ruano, J. G.; Sanz, G.; Toledo, M. A.; Urbano, A. Mild and regiospecific nuclear iodination of methoxybenzenes and naphthalenes with N-iodosuccinimide in acetonitrile. *Tetrahedron Lett.* **1996**, *37*, 4081–4084.

[38] Yuan, K.; Xu, Y. Z.; Uihlein, J.; Brunklaus, G.; Shi, L.; Heiderhoff, R.; Que, M. M.; Forster, M.; Chassé, T.; Pichler, T. et al. Straightforward generation of pillared, microporous graphene frameworks for use in supercapacitors. *Adv. Mater.* **2015**, *27*, 6714–6721.

[39] Vinod, K.; Jadhav, S. D.; Hariharan, M. Room temperature phosphorescence in crystalline iodinated eumelanin monomer. *Chem. - Eur. J.* **2024**, *30*, e202400499.

[40] Cheng, W. X.; Fan, F. F.; Zhang, Y.; Pei, Z. C.; Wang, W. J.; Pei, Y. X. A facile approach for fabrication of core-shell magnetic molecularly imprinted nanospheres towards hypericin. *Polymers* **2017**, *9*, 135.

[41] Choi, W. O.; Jung, Y. J.; Kim, M.; Kim, H.; Li, J. J.; Ko, H.; Lee, H. I.; Lee, H. J.; Lee, J. K. Substituent effects of fluorescein on photoredox initiating performance under visible light. *ACS Omega* **2023**, *8*, 40277–40286.

[42] Braslavsky, S. E. Glossary of terms used in photochemistry, 3rd edition. *Pure Appl. Chem.* **2007**, *79*, 293–465.
[43] Wegner, E. E.; Adamson, A. W. Photochemistry of complex ions. III. Absolute quantum yields for the photolysis of some aqueous chromium(III) complexes. Chemical actinometry in the long wavelength visible region. *J. Am. Chem. Soc.* **1966**, *88*, 394–404.
[44] Cismesia, M. A.; Yoon, T. P. Characterizing chain processes in visible light photoredox catalysis. *Chem. Sci.* **2015**, *6*, 5426–5434.
[45] Avens, H. J.; Bowman, C. N. Mechanism of cyclic dye regeneration during eosin-sensitized photoinitiation in the presence of polymerization inhibitors. *J. Polym. Sci. Part A: Polym. Chem.* **2009**, *47*, 6083–6094.
[46] Odian, G. *Principles of Polymerization*; 3rd ed. John Wiley & Sons, Inc: New York, 1991.
[47] Fleming, G. R.; Knight, A. W. E.; Morris, J. M.; Morrison, R. J. S.; Robinson, G. W. Picosecond fluorescence studies of xanthene dyes. *J. Am. Chem. Soc.* **1977**, *99*, 4306–4311.
[48] Romero, N. A.; Nicewicz, D. A. Organic photoredox catalysis. *Chem. Rev.* **2016**, *116*, 10075–10166.
[49] Yoon, J.; Jung, Y. J.; Yoon, J. B.; Damodar, K.; Kim, H.; Shin, M.; Seo, M.; Cho, D. W.; Lee, J. T.; Lee, J. K. The heavy-atom effect on xanthene dyes for photopolymerization by visible light. *Polym. Chem.* **2019**, *10*, 5737–5742.
[50] Cai, S. Z.; Ma, H. L.; Shi, H. F.; Wang, H.; Wang, X.; Xiao, L. X.; Ye, W. P.; Huang, K. W.; Cao, X. D.; Gan, N. et al. Enabling long-lived organic room temperature phosphorescence in polymers by subunit interlocking. *Nat. Commun.* **2019**, *10*, 4247.
[51] Rosspeintner, A.; Angulo, G.; Vauthey, E. Bimolecular photoinduced electron transfer beyond the diffusion limit: The Rehm-Weller experiment revisited with femtosecond time resolution. *J. Am. Chem. Soc.* **2014**, *136*, 2026–2032.
[52] Turró, C.; Zaleski, J. M.; Karabatsos, Y. M.; Nocera, D. G. Bimolecular electron transfer in the Marcus inverted region. *J. Am. Chem. Soc.* **1996**, *118*, 6060–6067.
[53] Brugh, A. M.; Forbes, M. D. E. Anomalous chemically induced electron spin polarization in proton-coupled electron transfer reactions: Insight into radical pair dynamics. *Chem. Sci.* **2020**, *11*, 6268–6274.

This is an open access article under the terms of the Creative Commons Attribution 4.0 International License (CC BY 4.0, https://creativecommons.org/licenses/by/4.0/).

© The Author(s) 2026. Published by Tsinghua University Press.